ADVANCED MATERIALS
www.advmat.de

# Design Principles of Quinone Redox Systems for Advanced Sulfide Solid-State Organic Lithium Metal Batteries

*Xiaodong Lin,* Petru Apostol, Hewei Xu, Vasudeva Rao Bakuru, Xiaolong Guo, Zehan Chen, Darsi Rambabu, Shubhadeep Pal, Da Tie, Yan Zhang, Xinlong Xie, Seung-Gi Kim, Yi Li, Zhao Li, Mengyuan Du, Shanshan Yan, Xiaozhe Zhang, Ruming Yuan, Mingsen Zheng, Fernand Gauthy, Vincent Finsy, Jianxin Zou, Jean-François Gohy, Quanfeng Dong, and Alexandru Vlad**

**The emergence of solid-state battery technology presents a potential solution to the dissolution challenges of high-capacity small molecule quinone redox systems. Nonetheless, the successful integration of argyrodite-type $Li_6PS_5Cl$, the most promising solid-state electrolyte system, and quinone redox systems remains elusive due to their inherent reactivity. Here, a library of quinone derivatives is selected as model electrode materials to ascertain the critical descriptors governing the (electro)chemical compatibility and subsequently the performances of $Li_6PS_5Cl$-based solid-state organic lithium metal batteries (LMBs). Compatibility is attained if the lowest unoccupied molecular orbital level of the quinone derivative is sufficiently higher than the highest occupied molecular orbital level of $Li_6PS_5Cl$. The energy difference is demonstrated to be critical in ensuring chemical compatibility during composite electrode preparation and enable high-efficiency operation of solid-state organic LMBs. Considering these findings, a general principle is proposed for the selection of quinone derivatives to be integrated with $Li_6PS_5Cl$, and two solid-state organic LMBs, based on 2,5-diamino-1,4-benzoquinone and 2,3,5,6-tetraamino-1,4-benzoquinone, are successfully developed and tested for the first time. Validating critical factors for the design of organic battery electrode materials is expected to pave the way for advancing the development of high-efficiency and long cycle life solid-state organic batteries based on sulfides electrolytes.**

## 1. Introduction

Organic electrode materials are emerging as a promising option for future electrochemical energy storage devices due to their attractive characteristics, including the inherent natural abundance of constituent elements, sustainability, and environmental friendliness.[1] Among the currently available organic electrode materials, small molecule quinone derivatives stand out as exceptionally promising candidates due to their high theoretical specific energy, fast reaction kinetics and structural tunability.[2] Nevertheless, despite these advantages, their very high solubility in liquid electrolytes engenders severe shuttling effect, leading to rapid capacity deterioration and consequently restricting their practical applications.[2] To address this issue, several strategies have been proposed, such as polymerization,[3] design of molecular structure,[4] incorporation of ionic groups,[5] separator coating to block shuttling,[6] and anchoring with insoluble conductive backbone.[7] Although these approaches

X. Lin, P. Apostol, H. Xu, V. R. Bakuru, X. Guo, Z. Chen, D. Rambabu, S. Pal, D. Tie, Y. Zhang, S.-G. Kim, Y. Li, Z. Li, M. Du, S. Yan, X. Zhang, J.-F. Gohy, A. Vlad
Institute of Condensed Matter and Nanosciences
Université Catholique de Louvain
Louvain-la-Neuve B-1348, Belgium
E-mail: xiaodong.lin@uclouvain.be; alexandru.vlad@uclouvain.be

The ORCID identification number(s) for the author(s) of this article can be found under https://doi.org/10.1002/adma.202312908



**DOI: 10.1002/adma.202312908**

X. Xie, Z. Li, J. Zou
National Engineering Research Center of Light Alloy Net Forming
State Key Laboratory of Metal Matrix Composite
Center of Hydrogen Science
School of Materials Science and Engineering
Shanghai Jiao Tong University
Shanghai 200240, China

R. Yuan, M. Zheng, Q. Dong
State Key Laboratory of Physical Chemistry of Solid Surfaces
Department of Chemistry
College of Chemistry and Chemical Engineering
Xiamen University
Xiamen 361005, China

effectively diminish the solubility of quinone derivatives, they simultaneously elevate the intricacy of synthesis, augment the fabrication costs, and increase the molecular weight that is inversely proportional to the gravimetric specific capacity. Moreover, most of these strategies only partially alleviate rather than eliminate the fundamental concern of quinone materials solubilization. Therefore, the development of quinone-based organic batteries still has a long way to go.

With the advent of all-solid-state battery technology, the application of quinone derivatives has been revitalized, as the solid-state electrolyte (SSE) technology has the potential to fundamentally address the dissolution challenge.[8] Among the available SSE classes, argyrodite $Li_6PS_5Cl$ (LPSCl) emerges as the most promising SSE system because of its high ionic conductivity, comparable to liquid electrolytes, low-temperature processability, and good compatibility with lithium metal compared to other sulfide SSEs.[9] The integration of quinone-based electrode materials and LPSCl is thus expected to enable the development of solid-state organic batteries with high energy density, safety and sustainability. However, the application of small molecules quinone systems in LPSCl-based solid-state lithium metal batteries (LMBs) remains poorly explored. Although two polycyclic quinone molecules, and namely pyrene-4,5,9,10-tetraone (PTO) and 5,7,12,14-pentacenetetrone (PT), have demonstrated applicability with $\beta$-$Li_3PS_4$ and the glass-ceramic $70Li_2S$-$30P_2S_5$ SSEs at elevated temperatures,[10] thus far, there have been no successful documentation cases of all-solid-state organic LMBs employing LPSCl and low molecular weight quinone derivatives (especially monocyclic quinones) as electrode materials, which may be due to their intrinsic reactivity and chemical incompatibility.

Regarding the reactivity of quinone derivatives with sulfide electrolytes, there are currently two viewpoints, with no unified consensus. Song et al.[11] explained the reactivity on the basis of hard and soft acid – base (HSAB) theory: suggesting that as a hard base, O of $H_2O$ for example, preferentially attacks the hard acid P of the sulfide electrolyte and replaces the soft base S, supported by the easy deliquescence of sulfide electrolytes. Similarly, they suggested that the hard base O of carbonyl in the discharged state (C—$O^-$) will interact with the hard acid P, hindering the recovery of C—$O^-$ to C═O during charging. Therefore, they proposed that organodisulfides such as poly(trithiocyanuric acid) (PTTCA), with "softer" "S—S" bonds, are more compatible with sulfide electrolytes, enabling the realization of a room-temperature solid-state battery based on $Li_7P_3S_{11}$ electrolyte and an organic polymer electrode material. Ji et al.[12] proposed a different viewpoint, attributing the reactivity of quinone small molecules with sulfide electrolytes to the nucleophilic attack on the redox center of the quinone molecule by the $PS_4^{3-}$ unit of the sulfide electrolyte, resulting in the generation of unidentified products. They proposed poly-(anthraquinonyl sulfide)-graphene (PAQS-G) nanocomposite as organic electrode material to inhibit the nucleophilic attack of $PS_4^{3-}$ on the carbonyl center by chemically shielding it with the inherent steric effect of the polymer framework, thus enhancing the compatibility with LPSCl electrolyte. Ultimately, they achieved a high-temperature solid-state battery based on LPSCl electrolyte and a quinone-based organic polymer electrode material. While both studies proposed effective strategies to enhance the chemical compatibility of sulfide electrolytes with organic electrode materials, the specific reaction products of sulfide electrolytes with quinone derivatives remains unidentified, the mechanistic insight remains under debate, and the application of small molecular weight quinone derivatives in room-temperature solid-state batteries based on LPSCl electrolyte remained unexplored.

From a chemical perspective, the reactivity between a quinone derivative and LPSCl may arise due to disparity in their redox potential.[13] For example, *p*-benzoquinone (BQ) has a higher redox potential as compared to the LPSCl, making it capable of oxidizing LPSCl.[13] In this scenario, the electron is transferred from the highest occupied molecular orbital (HOMO) of LPSCl to the lowest unoccupied molecular orbital (LUMO) of BQ.[14] Building upon this principle, we hypothesize that adjusting the LUMO energy level of quinone-based molecules could potentially regulate their reactivity with LPSCl, thus enabling their viable application as electrode materials in LPSCl-based solid-state batteries.

To verify this, we explore a suit of small molecular weight quinone derivatives with structurally similar features but varying LUMO energy levels as a model electrode material system, to explore the effect of LUMO energy levels on the reactivity between quinones and LPSCl, as well as the consequent electrochemical behaviors of all-solid-state organic batteries (**Figure 1**). We show that an increase in the energy level difference between the LUMO of quinine system and the HOMO of LPSCl results in a gradual reduction in their reactivity. Consequently, the material utilization of all-solid-state organic batteries exhibits gradual enhancement. Beyond a specific energy level difference, characterized as the threshold value, the interaction between the quinones and LPSCl becomes negligible, enabling all-solid-state organic batteries to achieve nearly complete material utilization. Based on these findings, we propose a design principle for quinone derivatives electrode materials integration with LPSCl SSE for solid-state batteries based on the LUMO energy level, and report for the first time two systems that can be used in LPSCl-based solid-state LMBs — 2,5-diamino-1,4-benzoquinone (DABQ) and 2,3,5,6-tetraamino-1,4-benzoquinone (TABQ). Among, the LPSCl-based all-solid-state LMB with TABQ as the electrode material exhibited excellent cycling and rate performances as well as a material-level energy density of up to 718 Wh $kg^{-1}$ at an operation temperature of 25 °C. We anticipate that the identification of these key designing descriptors will facilitate the application and development of small quinone-based molecules or other small organic molecules in next-generation all-solid-state organic batteries.

## 2. Results and Discussion

### 2.1. Selection of Quinone-Based Small Molecule Libraries

Considering that factors like steric hindrance and structural/volumetric variability may also impact the reactivity between quinone derivatives and LPSCl, we employed BQ as a molecular template for the selection of quinones sharing analogous structures but featuring varying LUMO energy levels.

F. Gauthy, V. Finsy
Syensqo SA
Battery Materials Platform
Solid State Battery Applicability Laboratory
Rue de la Fusée, 98, Brussels 1130, Belgium

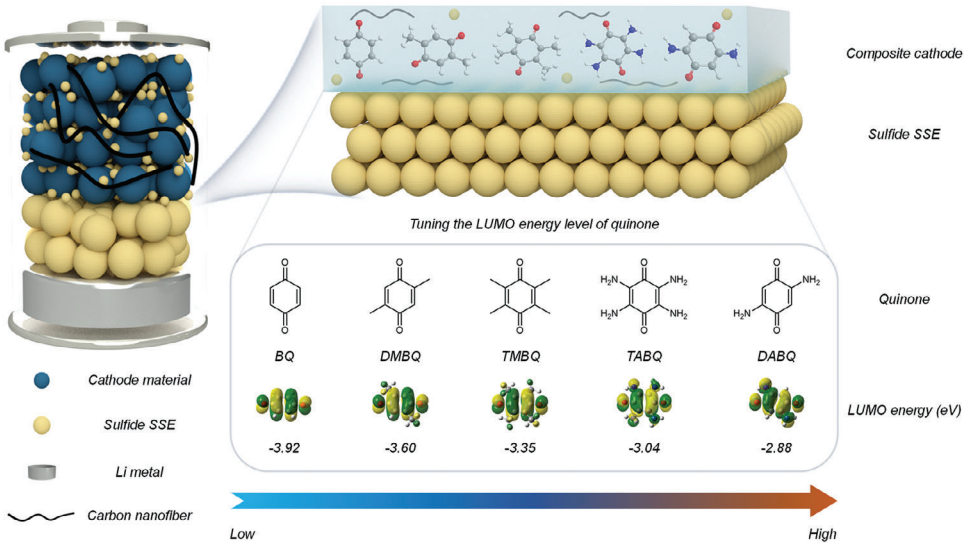


**Figure 1.** The rationale of this work. (Left) – Schematics of the solid-state organic battery construct applied in this work. (Right) Not all quinone redox systems are compatible with LPSCl solid electrolyte, with tuning the LUMO energy level of organic molecules rationalized for application in LPSCl-based all-solid-state LMBs.

It is widely recognized that the electron cloud density of organic molecules can be finely tuned by introducing electron-donating or electron-withdrawing groups, allowing for modulating the redox potentials.[1d,2c,5b,15] As previously discussed, BQ's ability to oxidize LPSCl stems from its higher redox potential compared to LPSCl.[13] To mitigate the reactivity between quinones and LPSCl, it is thus imperative to lower the redox potential of the quinone derived system. This entails introducing electron-donating groups to enhance the electron cloud density of quinone-based molecules. In the realm of organic chemistry, methyl (—$CH_3$) and amino (—$NH_2$) are common electron-donating groups, classified as weak and strong electron donors, respectively.[1d,2c] They can variably decrease the redox potential of organic molecules.[1d,2c] Moreover, these substituent groups are relatively small which would not induce significant steric hindrance effects. Given these considerations, we selected dimethyl/diamino-substituted and tetramethyl/tetraamino-substituted BQ molecules, specifically 2,5-dimethyl-1,4-benzoquinone (DMBQ), 2,5-diamino-1,4-benzoquinone (DABQ), 2,3,5,6-tetramethyl-1,4-benzoquinone (TMBQ), and 2,3,5,6-tetraamino-1,4-benzoquinone (TABQ), which together with BQ form a library of quinone-based small molecules, serving as a model electrode material system for this study.

As depicted in Figure 1, DFT calculations reveal the LUMO energy levels of BQ, DMBQ, TMBQ, TABQ, and DABQ to be −3.92, −3.60, −3.35, −3.04, and −2.88 eV, respectively. Since —$NH_2$ groups exhibit higher electron-donating effect compared to —$CH_3$ groups, both DABQ and TABQ have a substantially higher LUMO energy level than DMBQ and TMBQ. Notably, in contrast to the scenario involving —$CH_3$ substituents (where the electron-donating effect of four —$CH_3$ groups surpasses that of two —$CH_3$ groups, resulting in a higher LUMO energy level for TMBQ relative to DMBQ), DABQ, which incorporates two —$NH_2$ groups, exhibits a higher LUMO energy level than TABQ, that contains four —$NH_2$ groups. This anomaly arises because —$NH_2$ acts as a $\pi$ donor and as a sigma acceptor simultaneously, thereby inducing both electron-donating and electron-withdrawing effects.[2c] Generally, the electron-donating conjugation effect of —$NH_2$ outweighs its electron-withdrawing effect, leading to an overall electron-donating effect. In the case of DABQ, both —$NH_2$ groups can function as $\pi$ donors to conjugate with the *p*-benzoquinone segment (see Figure S1, Supporting Information). In contrast, for TABQ, as shown in Figure S2, Supporting Information, only two of the four —$NH_2$ groups engage in conjugation with the *p*-benzoquinone segment as $\pi$ donors, while the remaining two —$NH_2$ groups exhibit electron-withdrawing effects solely as sigma acceptors. Consequently, the electron cloud density of the *p*-benzoquinone segment in TABQ is lower than that of the *p*-benzoquinone segment in DABQ. This results in the LUMO energy level of TABQ being lower than that of DABQ, signifying that the reduction potential (i.e., discharge voltage plateau) of TABQ is higher than that of DABQ, which will be demonstrated and discussed latter.

### 2.2. LUMO-Dependent Reactivity of Quinone Molecules toward LPSCl SSE

To assess the chemical reactivity and stability between the selected quinones and LPSCl, a series of characterization techniques including scanning electron microscopy (SEM), X-ray diffraction (XRD), Fourier transform infrared (FTIR) spectroscopy and X-ray photoelectron spectroscopy (XPS) were employed. **Figure 2a** displays the optical photographs of LPSCl, five selected quinones, and their corresponding mixtures with LPSCl. Upon mixing for only 1 min, the colors of BQ, DMBQ, and TMBQ dramatically changed from their original brownish, yellow, and golden yellow shades to dark green, green, and light green, respectively. With prolonged grinding, these colors transitioned further to earthy yellow, earthy yellow, and green

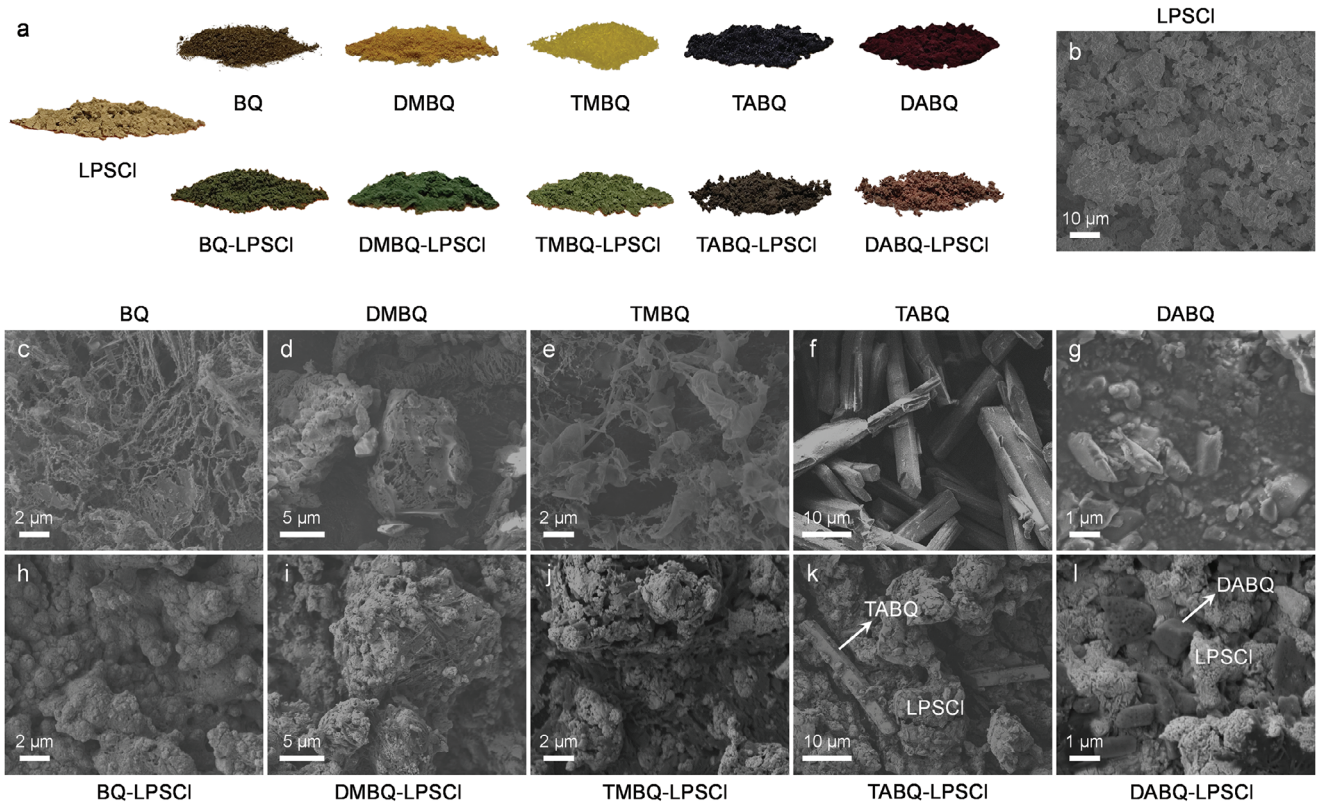


**Figure 2.** Chemical stability of quinone systems with LPSCl. a) Optical photographs and b–l) SEM images of pristine LPSCl (b), BQ (c), DMBQ (d), TMBQ (e), TABQ (f), DABQ (g) along with the BQ-LPSCl (h), DMBQ-LPSCl (i), TMBQ-LPSCl (j), TABQ-LPSCl (k) and DABQ-LPSCl (l) grinded powders.

(refer to Figure S3, Supporting Information), respectively. These color changes suggest strong chemical reactivity between BQ, DMBQ, TMBQ, and LPSCl. Conversely, the colors of TABQ and DABQ did not change significantly after mixing with the LPSCl; only a slight color lightening was observed, indicating negligible reactivity and good chemical stability between TABQ/DABQ and LPSCl. The color variation during the hand grinding process allowed us to roughly estimate the reactivity of the studied quinones with the LPSCl, and correlate this with the LUMO energy levels. We observed that as the LUMO energy level increased, the reactivity between the quinone and LPSCl gradually decreased. When the LUMO energy level reached a certain threshold, the reactivity of quinone-based molecules with the LPSCl SSE became negligible. Thus, we postulate that the reactivity of quinone-based molecules with LPSCl predominantly relies on their respective LUMO energy levels.

The microstructure of the LPSCl, selected quinones, and their mixtures with LPSCl was next analyzed using SEM (Figure 2b–l). The size of the pristine LPSCl particles predominantly range between 1 and 10 μm, with larger fragments primarily comprising secondary assemblies of smaller ones (Figure 2b). The pristine morphology of the five studied quinones is variable: BQ appears as a nanowire structure (Figure 2c), DMBQ exhibits a comb-like structure assembled out of nanowires (Figure 2d), TMBQ manifests a sheet-like structure (Figure 2e), TABQ displays a rod structure (Figure 2f), and DABQ demonstrates a granular structure formed from the accumulation of lamellar particles (Figure 2g).[2c] Upon integration with the LPSCl, the microstructures of BQ, DMBQ, and TMBQ undergo severe damage, with their pristine state morphology structures barely identifiable (Figure 2h–j). In contrast, TABQ and DABQ maintain well their original microstructures after blending with LPSCl (Figure 2k,l). The SEM analysis corroborates the reactivity of BQ, DMBQ, and TMBQ with the LPSCl, while highlighting the chemical stability between TABQ/DABQ and LPSCl.

To gain insight into the reaction mechanism of BQ, DMBQ, and TMBQ with LPSCl, and to validate the chemical stability of TABQ and DABQ with LPSCl SSE, we carried out additional physico-chemical and composition analysis. The XRD results (Figures S4–S6, Supporting Information) revealed a substantial crystalline structure degradation for BQ, DMBQ, and TMBQ upon mixing with LPSCl ($n_{quinone}$ : $n_{LPSCl}$ ≈ 1:2), indicating damage to the pristine crystallinity and the formation of amorphous species. On the contrary, TABQ (Figure S7, Supporting Information) and DABQ (Figure S8, Supporting Information) were found to preserve the crystallinity after mixing with LPSCl under identical conditions, underscoring their chemical stability with LPSCl. Since XRD was unable to detect amorphous species, we complemented our analysis using FTIR and XPS. The FTIR results displayed in **Figure 3**a and Figures S9–S12, Supporting Information revealed considerable changes in the absorption bands of BQ/DMBQ/TMBQ when mixed with LPSCl, showing disappeared or diminished C═O functional group stretching vibrations (≈1670 $cm^{-1}$), emergence of C—$O^-Li^+$ functional group stretching vibrations (≈1200 $cm^{-1}$), and appearance of C═C aromatic ring stretching vibrations (≈1500 $cm^{-1}$).[2c,5b]

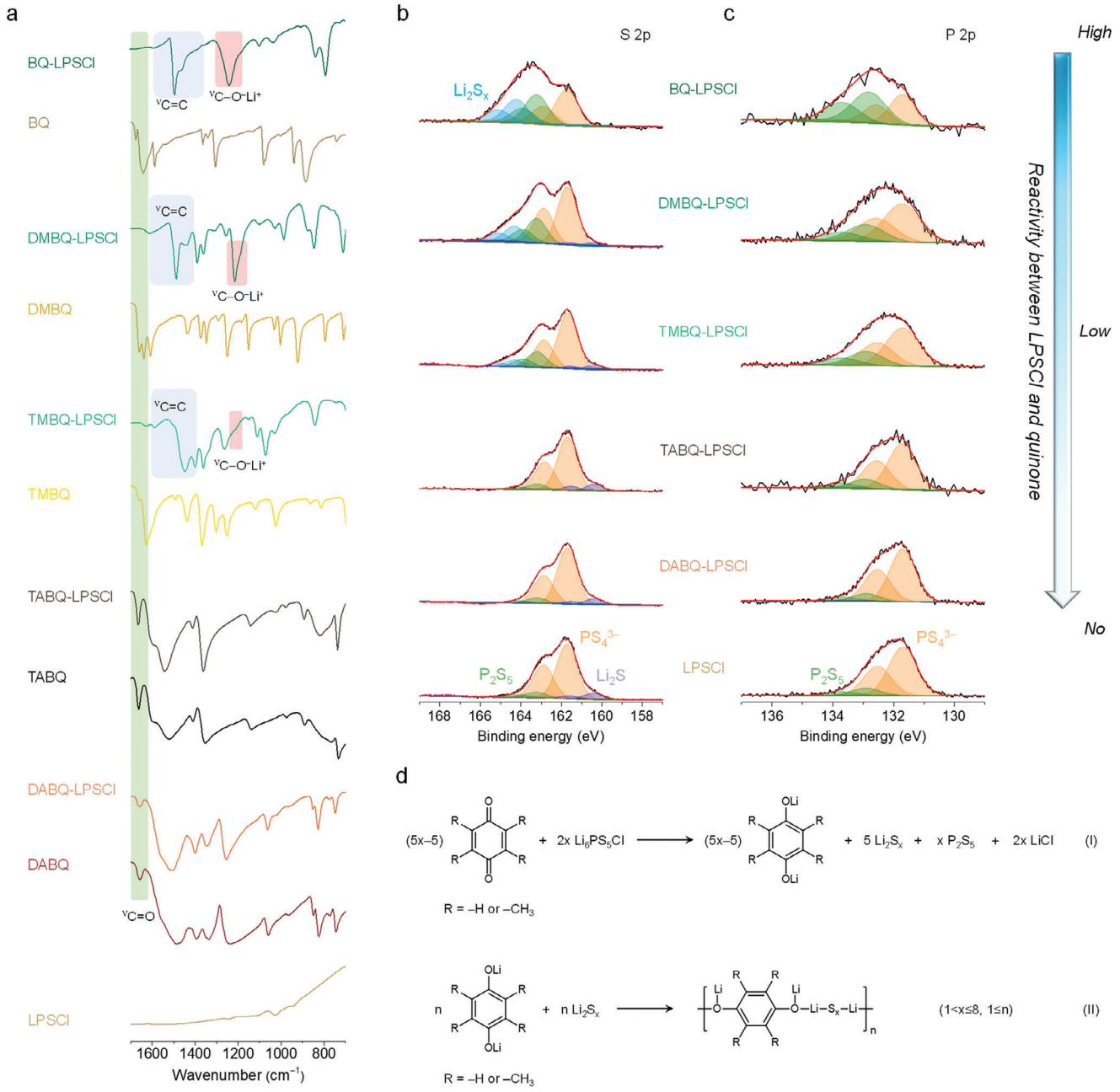


**Figure 3.** Reactivity and reaction products analysis of quinone-LPSCl systems. a) Comparison of the FTIR spectra of LPSCl, BQ, DMBQ, TMBQ, TABQ, DABQ and the BQ-LPSCl, DMBQ-LPSCl, TMBQ-LPSCl, TABQ-LPSCl and DABQ-LPSCl mixtures. b,c) Comparison of the S 2p (b) and P 2p (c) XPS spectra of LPSCl and the BQ-LPSCl, DMBQ-LPSCl, TMBQ-LPSCl, TABQ-LPSCl and DABQ-LPSCl mixtures. The existence of $Li_2S$ and $P_2S_5$ species in the pristine LPSCl might be attributed to the residual of the precursor materials employed during the synthesis process. d) Possible reaction pathways between LPSCl and BQ/DMBQ/TMBQ.

These observations suggest the reduction of BQ, DMBQ, and TMBQ to $Li_2$BQ, $Li_2$DMBQ, and $Li_2$TMBQ upon interaction with LPSCl, which is further corroborated by the $^1$H and $^{13}$C nuclear magnetic resonance (NMR) spectroscopy (refer to Figures S13–S20, Supporting Information) and high-performance liquid chromatography-mass spectrometry (HPLC-MS) analyses (refer to Figures S21–S27 and Tables S1–S7, Supporting Information). Moreover, XPS (Figure 3b,c and Figure S28, Supporting Information) also revealed the oxidative decomposition of LPSCl into species such as $Li_2S_x$ ($1 < x \leq 8$), $P_2S_5$, and LiCl subsequent to its combination with BQ, DMBQ, and TMBQ. Based on these findings, we suggest a possible reaction mechanism (as illustrated in Equation (I) in Figure 3d) elucidating the potential interactions between the BQ/DMBQ/TMBQ and the LPSCl.

Interesting to note, only the valence state of the sulfur element in LPSCl undergoes alteration. Thus, we speculate that the

reactivity of quinone-based molecules with LPSCl primarily hinges on their capability to oxidize the divalent sulfur anion ($S^{2-}$). To verify this hypothesis, we conducted a control experiment by mixing BQ with $Li_2S$, yielding similar color change (Figure S29, Supporting Information), FTIR spectra (Figures S30 and S31, Supporting Information), NMR spectra (Figures S32 and S33, Supporting Information) and HPLC-MS (Figure S34 and Table S8, Supporting Information) results to those observed when BQ interacted with the LPSCl, which indicates analogous reaction mechanisms as depicted in Equation (I') in Figure S35, Supporting Information. The consistent colors of the BQ-LPSCl/BQ-$Li_2S$ mixtures and potential reaction products (Figure S36, Supporting Information), along with the reversed color change observed when $Li_2BQ$ is exposed to air (oxidized by oxygen, refer to discussion in Figure S37, Supporting Information), compared to the BQ-LPSCl/BQ-$Li_2S$ grinding process (Figures S3, S9, S29, and S30, Supporting Information), further support the reliability of the proposed reaction pathway. It is worth mentioning that in our earlier investigations on liquid electrolyte additives for lithium-sulfur batteries, we found that $Li_2BQ$ engages with $Li_2S_x$ to create polymeric structures, a process supported by both theoretical calculations and experimental evidences.[13d] Hence, we suggest that in the BQ-LPSCl and BQ-$Li_2S$ mixture system, the $Li_2BQ$ and $Li_2S_x$ reaction products, as illustrated in both Equation (I) in Figure 3d and Equation (I') in Figure S35, Supporting Information, may spontaneously combine to form polymer species, as shown in Equation (II) and (II') in Figure 3d and Figure S35, Supporting Information, respectively. This was subsequently confirmed by a series of HPLC-MS analyses (See detailed analysis and discussion in Figures S38–S45 and Tables S9–S16, Supporting Information). Additionally, the FTIR (Figure 3a, Figures S46 and S47, Supporting Information), NMR (Figures S48–S51, Supporting Information) and XPS (Figure 3b,c and Figure S28, Supporting Information) results reaffirm the excellent chemical stability existing between TABQ/DABQ and LPSCl.

### 2.3. Electrochemical Performance of Quinone-Based All-Solid-State Organic LMBs

To explore the impact of quinone-based molecules' chemical reactivity with LPSCl SSE on solid-state LMB performance, we conducted comparative tests using the selected quinones as active electrode material in a Li | LPSCl | quinone-LPSCl-carbon nanofiber (CNF) cell configuration. It is widely recognized that adequate ionic and electronic conductivities are pivotal in facilitating rapid and complete lithiation/de-lithiation electrochemical reactions of the active material within the composite electrode, which will result in minimal charge/discharge polarization, high-rate performance, and optimized discharge specific capacity (material utilization). To achieve this, we first assessed the solid-state LMB performances of the five quinone molecules using a relatively low active material mass loading ratio (e.g., quinone-LPSCl-CNF mass ratio of 15:70:15).

It is noteworthy that while LPSCl exhibits high room temperature ionic conductivity (≈3.8 mS $cm^{-1}$, Figure S52, Supporting Information); akin to many sulfide SSEs, it possesses a relatively narrow electrochemical stability window.[13b,c] Previous studies by Meng et al.[11b] and Wagemaker et al.[13c] demonstrated that LPSCl-C composite electrode, prepared through ball milling, could attain significant charge/discharge specific capacities within an operating voltage window of 0–4.2 V (versus $Li/Li^+$). Moreover, the capacity was maintained over subsequent cycles, underscoring the intrinsic reversible redox activity of LPSCl in a broad operating voltage range.[13b,c] Thus, the operating voltage window of the active material significantly influences the extent of LPSCl's redox reactions during cell cycling. Generally, if the operating voltage window of the active material exceeds the electrochemical stability window of LPSCl, it becomes challenging to completely prevent its redox during cycling, only reducing it instead. Previous studies have demonstrated that applying a thin layer of an electronically insulating yet lithium-ion-conducting surface coating, such as $LiNbO_3$, onto the active material surface effectively suppressed the sulfide SSE's decomposition.[16] The use of carbon nanofibers with lower specific surface areas instead of carbon nanoparticles with higher specific surface areas as conductive agents can also moderately mitigate sulfide SSE decomposition.[13b] Additionally, some studies also disclosed that sulfide-carbon mixtures prepared by hand grinding methods yield a significantly lower charge-discharge capacity compared to those prepared by ball milling methods.[8b,10b] This observation suggests that the preparation method of the composite electrode can also influences the extent of LPSCl's redox reaction during the charge-discharge cycles.

Given that the operating voltage windows of the quinones employed in this study partially exceed the electrochemical stability window of LPSCl, we utilized a mortar and pestle to prepare quinone-LPSCl-CNF composite electrode through a hand grinding method to minimize the redox reactions of the LPSCl. As illustrated in Figure S53, Supporting Information, our results demonstrate that the LPSCl-CNF composite electrode, prepared using the hand grinding method, indeed provides a negligible charge/discharge capacity (at a temperature of 25 °C) within the operating voltage range of the studied quinones. This capacity is significantly lower than that observed with the one prepared via the ball-milling method. Hence, we believe that the charge/discharge capacity of the quinone-LPSCl-CNF composite electrode, prepared by the hand grinding method and tested at 25 °C in this study, primarily arises from the lithiation/de-lithiation electrochemical redox reaction of the quinone-based molecules. Additionally, we do not rule out the possibility that a marginal capacity may stem from the redox reaction of LPSCl SSE.

To avoid the potential contribution of the LPSCl SSE's redox reactions to the capacity after long-term cycling as illustrated in previous study,[10b] we determined the material utilization of quinones by using the highest discharge specific capacity from the initial three cycles. As depicted in Figures S54–S56, Supporting Information, the discharge specific capacities of BQ, DMBQ, and TMBQ fall significantly below their theoretical specific capacities (i.e., 496, 394, and 327 mAh $g^{-1}$, calculated based on the two-electron redox process) at both, room temperature (25 °C) and high temperature (60 °C). Their respective highest attained discharge specific capacities at 25/60 °C are 106/103, 125/119, and 126/108 mAh $g^{-1}$, resulting in material utilizations of as low as 21.4%/20.8%, 31.7%/30.2%, and 38.5%/33%, respectively (**Figure 4a**). In sharp contrast, TABQ and DABQ

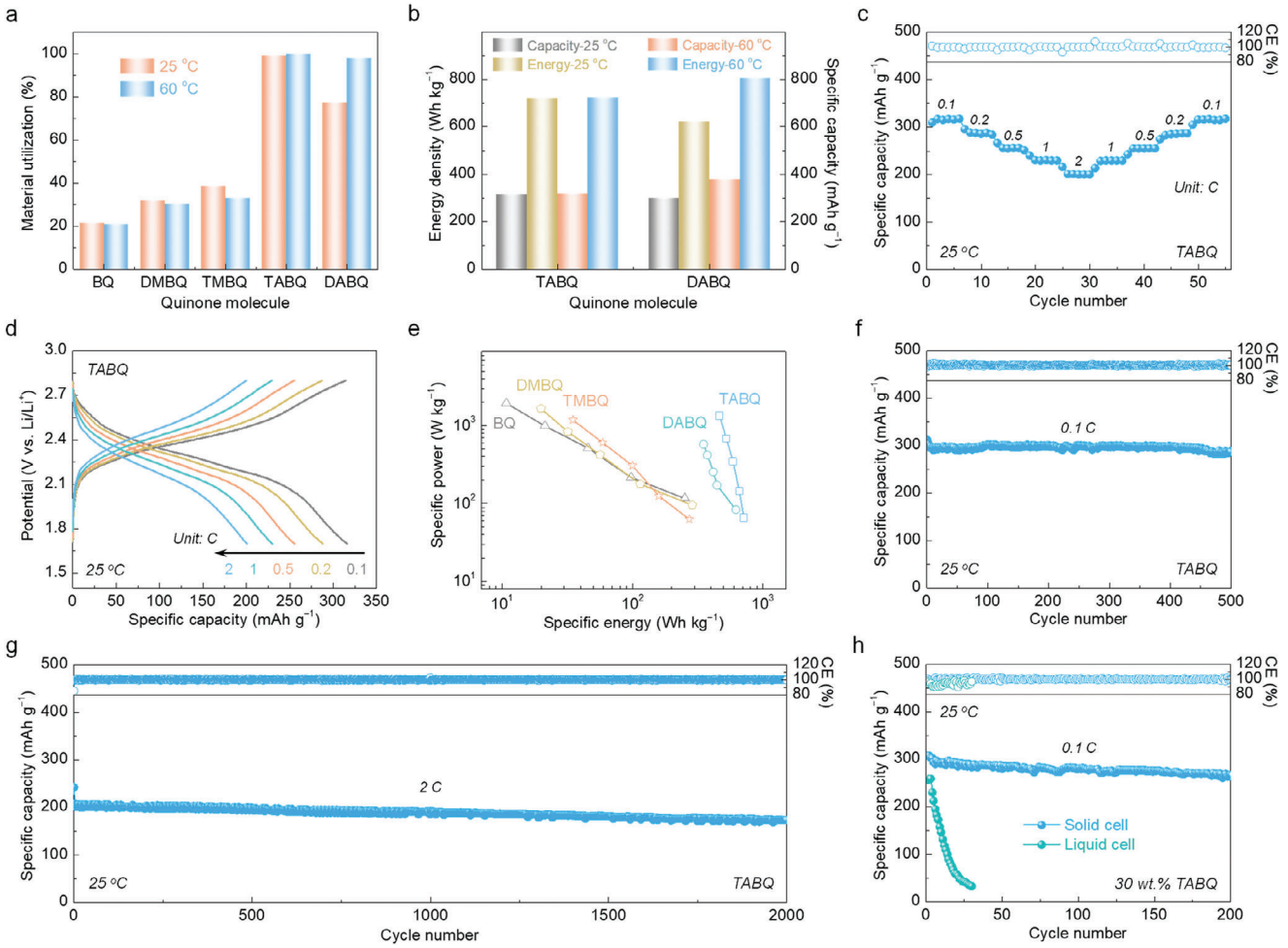


**Figure 4.** Electrochemical performance of quinone solid-state organic LMBs. a) Comparison of the material utilization for BQ, DMBQ, TMBQ, TABQ, and DABQ in LPSCl-based solid-state organic LMBs with the composite electrode mass ratio of $m_{quinone} : m_{LPSCl} : m_{CNF}$ = 15:70:15. b) Comparison of the specific discharge capacity and specific energy density of TABQ- and DABQ-based solid-state LMBs at 25 and 60 °C, with composite electrode mass ratio of $m_{quinone} : m_{LPSCl} : m_{CNF}$ = 15:70:15. c,d,f,g) The specific discharge capacity, Coulombic efficiency (c, f, g), and selected galvanostatic charge-discharge profiles (d) of the LPSCl-based solid-state cells using TABQ as the active electrode material; at (c, d) varying current rates from 0.1 to 2 C, and current rate of f) 0.1 C and g) 2 C with composite electrode mass ratios of (d–g) $m_{quinone} : m_{LPSCl} : m_{CNF}$ = 15:70:15. h) Comparison of the cycling stability of the TABQ solid-state electrolyte and liquid electrolyte cells at a current rate of 0.1 C.

exhibit much better material utilization at both 25 and 60 °C (Figure 4a). Specifically, TABQ approached its theoretical specific capacity (319 mAh $g^{-1}$, calculated based on the two-electron redox process), achieving 316 (Figure S57a, Supporting Information) and 318 mAh $g^{-1}$ (Figure S57b, Supporting Information) at 25 and 60 °C, respectively, with material utilization of 99% and 99.7% as well as specific energy density of 718 and 723 Wh $kg^{-1}$ (Figure 4b). While DABQ exhibits a lower discharge specific capacity of 300 mAh $g^{-1}$ at 25 °C (Figure S58a, Supporting Information), corresponding to a material utilization of ≈77.3% (theoretical capacity: 388 mAh $g^{-1}$, calculated based on the two-electron redox process) and a specific energy density of 622 Wh $kg^{-1}$ (Figure 4b). Nevertheless, it remarkably displays an increased discharge specific capacity of 379 mAh $g^{-1}$ at 60 °C (Figure S58b, Supporting Information), attaining an impressive material utilization of up to 97.7% and a high specific energy density of up to 803 Wh $kg^{-1}$ (Figure 4b). The significant variation in DABQ's material utilization at 25 and 60 °C may be related to the kinetics of its lithiation/de-lithiation electrochemical reactions. Notably, the charge/discharge polarization of DABQ is considerably higher at 25 °C compared to TABQ (Figure S59, Supporting Information). Upon elevating the temperature to 60 °C, DABQ experiences a substantial reduction in charge/discharge polarization (Figure S59, Supporting Information), suggesting an improvement in the kinetics of the lithiation/de-lithiation process and thus enhancing the material utilization. This differs notably from BQ, DMBQ, and TMBQ, where material utilization at 60 °C is reduced compared to 25 °C (Figure 4a). This reduction is attributed to the exacerbation of side reactions with the LPSCl (as discussed earlier) under high-temperature conditions, leading to diminished material utilization.

Considering the remarkable material utilization achieved with TABQ at room temperature, subsequent studies are concentrated on TABQ, as this work is focused on the development of

quinone-based molecules that can be applied to LPSCl-based SSE system for the construction of high-energy-density room-temperature all-solid-state organic LMBs. Figure 4c,d display the rate performance of TABQ solid-state organic cells at 25 °C. As the current rate is ramped from 0.1 to 2 C, the average discharge specific capacity experiences a slight decline, measuring 315, 288, 257, 231, and 203 mAh $g^{-1}$ at 0.1, 0.2, 0.5, 1, and 2 C, respectively. Upon reverting the current rate sequentially to 1, 0.5, 0.3, 0.2, and 0.1 C, the average discharge specific capacity restored to 226, 253, 283, and 314 mAh $g^{-1}$, respectively, demonstrating the excellent rate capability of the TABQ-based all-solid-state organic LMBs. Figure 4e presents the Ragone plot for the five studied quinone-based solid-state LMBs. DABQ and TABQ consistently demonstrate higher specific energies compared to BQ, DMBQ, and TMBQ at an equivalent specific power. Moreover, their specific energies remain relatively stable with increasing specific power, indicating excellent power characteristics. Particularly noteworthy is the outstanding performance of TABQ, which not only achieves the highest specific energy (718 Wh $kg^{-1}$) at a current rate of 0.1 C and 25 °C, but also attains a remarkable power density of ≈1340 W $kg^{-1}$ at a current rate of 2 C. Additionally, the TABQ-based solid-state cells also exhibit exceptional cycling stability at current rates of 0.1 and 2 C, maintaining 92% (Figure 4f and Figure S60, Supporting Information) and 72% (Figure 4g and Figure S61, Supporting Information) of the initial capacity after 500 and 2000 cycles, respectively. To further highlight the superiority of TABQ, we increased the mass ratio to 30 wt.%, that is, $m_{quinone} : m_{LPSCl} : m_{CNF}$ = 30:60:10 (Figure 4h and Figure S62, Supporting Information). It is worth noting that this ratio slightly exceeds the commonly used composite electrode mass ratio (i.e., $m_{quinone} : m_{SSE} : m_C$ = 20:70:10) in previous studies on quinone-based solid-state organic LMBs using other sulfide SSEs.[8b,10] As depicted in Figure 4h, the cell maintains excellent cycling stability at a current rate of 0.1 C, retaining 87% of its initial capacity after 200 cycles. These results sharply contrast with the rapid capacity degradation observed in a liquid electrolyte cell configuration, as illustrated in Figure 4h and Figure S63, Supporting Information, which emphasizes the potential of solid-state battery technology in addressing dissolution issues associated with highly soluble organic electrode materials such as quinone-based molecules.

Compared to inorganic solid-state LMBs, organic systems exhibit lower active material mass ratios and mass loading. This discrepancy primarily stems from the lower tap density, as well as lower electronic and ionic conductivity of organic electrode materials. Consequently, composite electrodes for organic solid-state LMBs require higher mass ratios of solid electrolyte and conductive carbon to ensure efficient electronic and ionic conduction. Reported values in the literature for the active material mass ratio and mass loading in organic small molecule-based solid-state LMBs are generally in the 20 wt.% and 0.5 mg $cm^{-2}$ maximum range, respectively (Table S17, Supporting Information). So far, the highest reported organic active material mass ratio and mass loading reach 40 wt.% and ≈1.07 mg $cm^{-2}$, respectively, however, achieved under a high temperature operation of 60 °C (refer to Table S17, Supporting Information). The low active material mass ratios and mass loading limits the areal capacity of current organic small molecule all-solid-state LMBs, typically lower than 0.5 mAh $cm^{-2}$. Clearly, further enhancements in the active material mass ratio and mass loading are imperative for advancing organic all-solid-state LMBs.

Nevertheless, we tested increased mass ratio and mass loading of TABQ to the maximum feasible extent. As depicted in Figure S64, Supporting Information, with a TABQ mass ratio of 30% and a corresponding mass loading of 2 mg $cm^{-2}$, a discharge specific capacity of ≈275 mAh $g^{-1}$ (≈82% material utilization) is achieved at a current rate of 0.1 C and a temperature of 25 °C. The resulting areal capacity reaches 0.55 mAh $cm^{-2}$, with 86% of the initial capacity retained after 100 cycles. Further elevating the TABQ mass loading to 4 mg $cm^{-2}$ yielded a specific capacity of 264 mAh $g^{-1}$ at a current rate of 0.05 C and 25 °C (Figure S65a, Supporting Information), attaining an impressive areal capacity of 1 mAh $cm^{-2}$—the highest reported in the realm of organic small molecule-based solid-state LMBs. However, at a current rate of 0.1 C, the capacity diminishes to 206 mAh $g^{-1}$, with 63% of the initial capacity maintained after 30 cycles (Figure S65b, Supporting Information). Elevating the operating temperature to 60 °C enables the all-solid-state organic LMB to attain a discharge specific capacity of up to 304 mAh $g^{-1}$ at a current rate of 0.1 C, with a corresponding areal capacity of up to 1.2 mAh $cm^{-2}$, and 73.5% of the initial capacity retained after 30 cycles (Figure S66, Supporting Information).

We also increased the mass ratio of TABQ to 40%. The corresponding solid-state LMB achieved a discharge specific capacity of ≈258 mAh $g^{-1}$ at a mass loading of 0.5 mg $cm^{-2}$, a current rate of 0.1 C, and a temperature of 25 °C, maintaining over 82% of the initial capacity after 110 cycles (Figure S67, Supporting Information). At an operating temperature of 60 °C, the cell achieved a discharge specific capacity of 212 mAh $g^{-1}$ at a current rate of 1 C, with over 70% of the initial capacity retained after 300 cycles (Figure S68, Supporting Information). Moreover, with a mass loading increased to 2 mg $cm^{-2}$, the TABQ-based all-solid-state LMB can still maintain a discharge specific capacity of 244 mAh $g^{-1}$ at a current rate of 0.1 C, with 89% of the initial capacity preserved after 25 cycles (Figure S69, Supporting Information).

Finally, increasing the mass ratio of TABQ to 50% resulted in suboptimal performances. Even at a low mass loading of 0.5 mg $cm^{-2}$, the cells achieved only a discharge specific capacity of ≈148 mAh $g^{-1}$ at a current rate of 0.1 C and a temperature of 25 °C, with more than 64% of its initial capacity retained after 100 cycles (Figure S70, Supporting Information). Elevating the operating temperature to 60 °C enhanced the performances significantly. At the same current rate and mass loading, the cell attained a discharge specific capacity of 262 mAh $g^{-1}$, with a material utilization of ≈82%, and preserved more than 85% of the initial capacity after 50 cycles (Figure S71, Supporting Information). Notably, this marks the highest active material mass ratio reported thus far for organic small molecule-based all-solid-state batteries. In short, TABQ-based all-solid-state LMBs demonstrate outstanding electrochemical performance at both room and elevated temperatures, even with increased active-material mass ratios and mass loadings. These performances surpass those of other reported organic small molecule-based all-solid-state LMB systems (Table S17, Supporting Information).

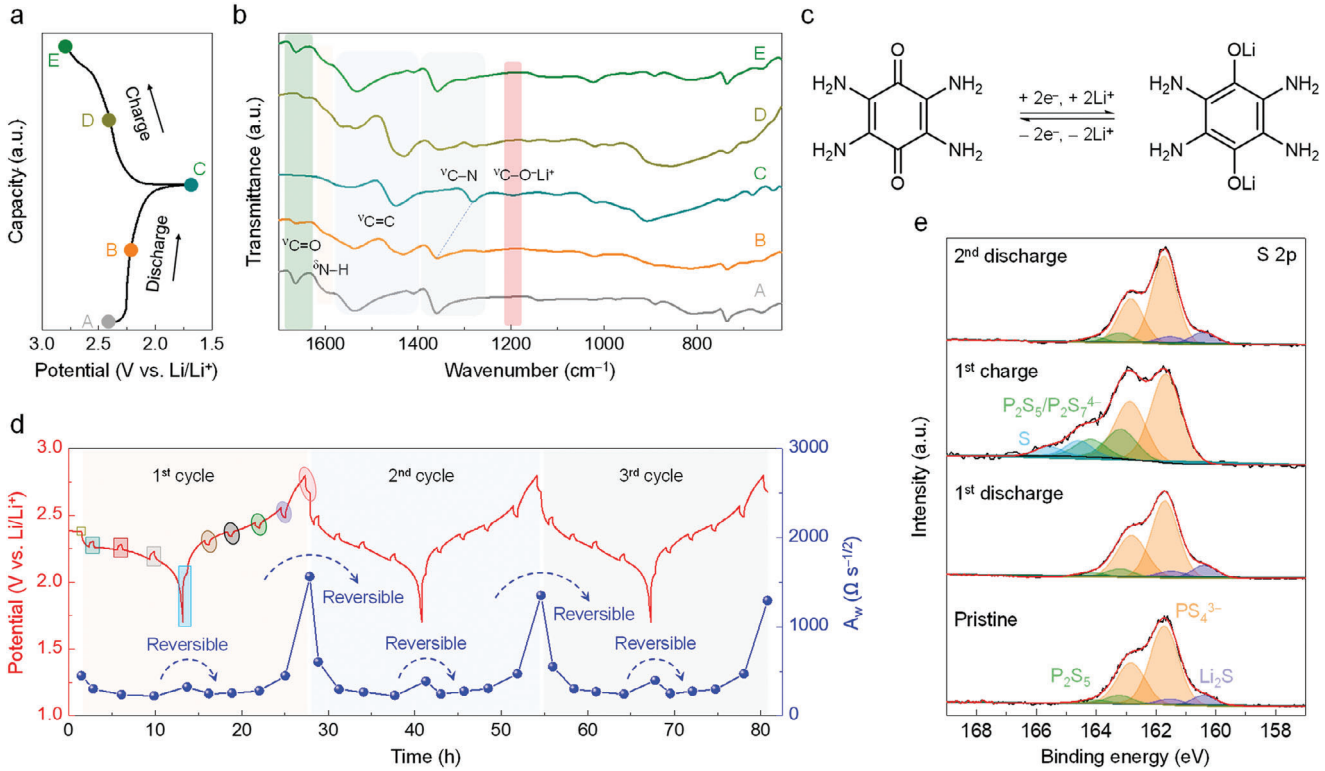


**Figure 5.** Redox mechanism analysis. a) Galvanostatic charge-discharge profile and the corresponding redox states selected for the ex situ FTIR characterization of the TABQ-LPSCl-CNF composite electrode and b) the corresponding FTIR survey of the redox process. c) Redox reaction of TABQ. d) Intermittent galvanostatic charge-discharge profile and the corresponding Warburg coefficient plot ($A_w$) extracted from the low-frequency EIS analysis for first three cycles. e) Ex situ XPS spectra of the TABQ-LPSCl-CNF composite electrode collected at different discharge and charge states.

### 2.4. Redox Mechanism and Electrode Reversibility Analysis

To gain deeper insights into the electrochemical mechanism and reversibility of TABQ's redox process in the LPSCl-based all-solid-state organic LMBs, ex situ FTIR analysis was conducted. **Figure** 5a,b illustrates the FTIR spectrum of the TABQ-LPSCl-CNF composite collected at five distinct states: pristine (A), half-discharged (B), fully discharged (C), half-charged (D), and fully-charged (E); enabling comparative FTIR spectra analysis. The C═O stretching vibration band (at ≈1670 $cm^{-1}$) gradually weakened and disappeared with the lithiation (discharge) progression, while the phenolate (C—O$^-$Li$^+$) stretching vibration band emerged at ≈1200 $cm^{-1}$ (more visible in Figure S72, Supporting Information). During the subsequent delithiation (charging) step, the C═O stretching band gradually reappeared, and simultaneously, the phenolate (C—O$^-$Li$^+$) stretching band gradually faded. The FTIR spectrum of the TABQ-LPSCl-CNF electrode after one complete cycle closely resembled that of the pristine sample. The FTIR results not only confirm the reversible two-electron redox reaction of TABQ (Figure 5c), but also highlight its significant capacity contribution throughout the charging and discharging process of the LPSCl-based solid-state organic LMB system.

The Warburg coefficient ($A_w$) within the low-frequency range of the electrochemical impedance spectroscopy (EIS) reflects the ionic diffusion resistance at the active material-electrolyte interface, thereby providing insights into the evolution of the electrode-electrolyte interface.[8b,10a] To examine the evolution of the TABQ-LPSCl interface, we conducted in situ EIS measurements over the course of the initial three cycles. Each EIS measurement was preceded by a 30-min resting period to ensure reaching close to equilibrium conditions. Figure 5d displays the intermittent galvanostatic charge-discharge profiles and $A_w$ derived from the low-frequency EIS (1.0–0.1 Hz) at selected potentials for these cycles (refer also to Figure S73, Supporting Information). In the first cycle, $A_w$ decreases from 451.7 Ω $s^{-1/2}$ at open circuit voltage (2.39 V) to 223.9 Ω $s^{-1/2}$ upon discharge to 2.15 V, then rises to 322.4 Ω $s^{-1/2}$ as the discharge continues to 1.7 V. Upon initiation of charging (1.7 to 2.28 V), $A_w$ marginally drops to 247.5 Ω $s^{-1/2}$. As the charging voltage progresses to 2.53 V, $A_w$ gradually returns to near the pristine state (449 Ω $s^{-1/2}$). At 2.8 V (beyond the LPSCl decomposition potential), $A_w$ significantly rises to 1561.4 Ω $s^{-1/2}$. Notably, during the second discharge, $A_w$ gradually recovers to the level at the end of the first discharge as the voltage reaches 1.7 V. Subsequently, it follows the same trend observed in the first cycle, repeating in the second and third cycles. The TABQ-LSPCl cells demonstrate thus reversible resistance evolution of the cathode-electrolyte interface within two distinct voltage regions. Specifically, the minor variations in $A_w$ observed within the OCV → 1.7 → 2.53 V range may be attributed mainly to the fluctuating lithium-ion conductivity of $Li_x$TABQ ($0 \le x \le 2$) at different lithiation levels.[10b] Additionally, the slight fluctuations in $A_w$ values occurring between 2.15 → 1.7 → 2.28 V may be linked to the marginal reduction of LPSCl

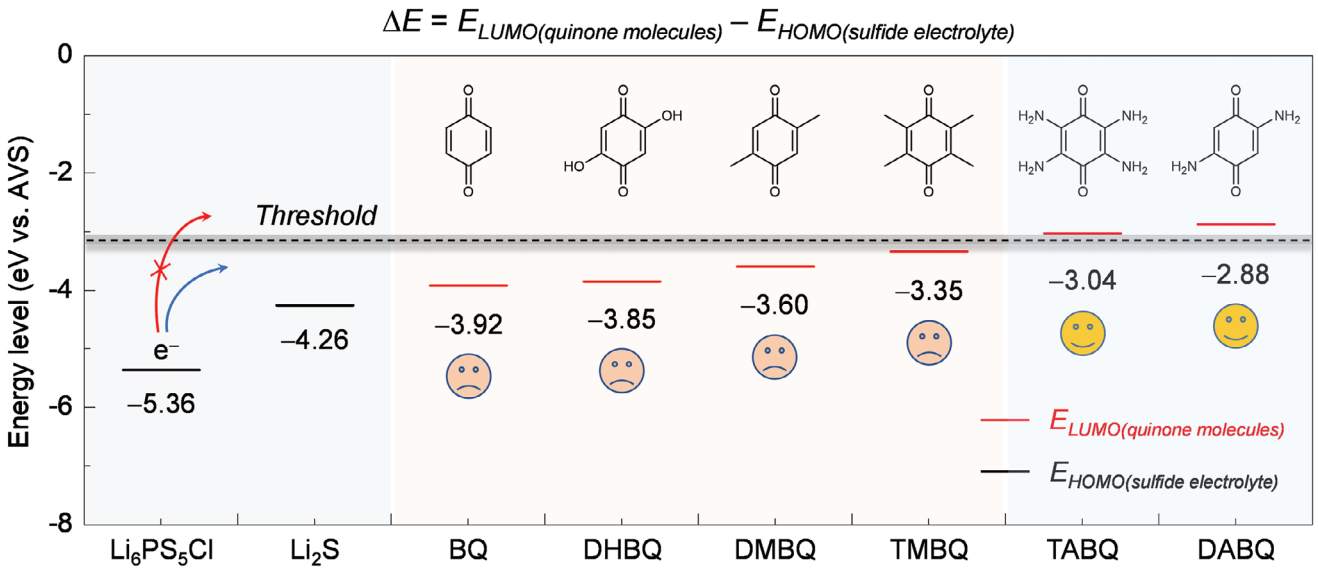


**Figure 6.** Designing principle of small organic molecules for LPSCl-based all-solid-state LMBs integration and efficient utilization.

and the subsequent reoxidation of its reduction products.[13b,c] In contrast, the substantial changes in $A_w$ values within the 2.53 → 2.8 → 2.43 V range primarily relate to the oxidation of a fraction of the LPSCl SSE and the reduction of its oxidized products.[13b,c] It is important to note that the discrepancy in $A_w$ between the fully discharged and fully charged states stems from two primary factors. First, it corresponds to the dissimilarity in LPSCl SSE decomposition levels during the discharge and charge processes, wherein the reductive decomposition extent at 1.7 V is significantly lower than the oxidative decomposition extent at 2.8 V. Second, it accounts for the varying ionic conductivity of the decomposition products, as prior literature on sulfide SSEs has reported superior ionic conductivity of the reductive decomposition products compared to the oxidative decomposition phases.[13b]

To further validate the reversibility of the oxidative decomposition products, XPS analysis was conducted on the TABQ-LPSCl-CNF composite in various states. As depicted in Figure 5e, compared to the S 2p XPS spectra of the pristine state, the enhancement of signals related to LPSCl reductive decomposition products (such as $Li_2S$) after the first discharge is subtle, suggesting a minimal or nearly negligible degree of SSE reduction at the end of discharge. Conversely, after the first charge, the disappearance of the $Li_2S$ signal and evident intensification of $P_2S_5$, along with the appearance of S signal, implies relatively higher degree of SSE oxidation. Moreover, besides the $S^{2-}$ remaining from the raw materials during the LPSCl synthesis that oxidizes to S, a segment of LPSCl undergoes oxidation and decomposes into S, LiCl, and $Li_3PS_4$.[13b,c] Further oxidative decomposition of $Li_3PS_4$ into $Li^+$, S, and $P_2S_5/P_2S_7^{4-}$ results in a sharp increase in $A_w$ value, ascribed to the poor ionic conductivity of S and $P_2S_5/P_2S_7^{4-}$ species.[13b,c] Following the second discharge, the S 2p XPS spectrum returns to a state akin to that after the first discharge. This recovery is mainly attributed to the reactivity of oxidative resistive products (S and $P_2S_5/P_2S_7^{4-}$), which can reform $Li_3PS_4$ with improved ionic conductivity during the discharge process.[13b,c] These results affirm the good reversibility of oxidative resistive products that favor the battery's long-term cycling.

### 2.5. Outlook and Designing Principle of Small Organic Molecules for $Li_6PS_5Cl$-Based All-Solid-State LMBs

It is worth mentioning that —$NH_2$ as a strong ligand, has the potential to impede the reaction between quinones (i.e., DABQ and TABQ) and the LPSCl through coordination or other interaction mechanisms. The 2,5-dihydroxy-1,4-benzoquinone (DHBQ) is a good control sample to exclude the effect of the —$NH_2$ strong ligand on the reactivity, since DHBQ also has a strong ligand moiety, the —OH substituent group, and its LUMO energy level (−3.85 eV, **Figure 6**) is close to that of BQ (−3.92 eV). Therefore, an investigation into the reactivity between DHBQ and LPSCl can elucidate whether the determining factor in the reactivity of quinone derivatives with LPSCl is the LUMO energy level or the presence of a strong ligand group.

To explore the reactivity of DHBQ with LPSCl, we conducted similar characterization tests and analyses. The FTIR results (Figures S74 and S75, Supporting Information) indicate the disappearance of the C═O stretching vibration at 1607 $cm^{-1}$ and the O—H stretching vibration at 3288 $cm^{-1}$ of DHBQ upon mixing with LPSCl. Conversely, a stretching vibration associated with C—O$^-$Li$^+$ emerges near 1267 $cm^{-1}$. Comparison of the FTIR spectra with those of lithium benzene-1,2,4,5-tetrakis(olate) ($Li_4$TOBQ) and lithium 2,5-dihydroxybenzoquinonate ($Li_2$DOBQ) suggests the reduction of DHBQ to $Li_4$TOBQ by LPSCl during the mixing process. NMR (Figures S76 and S77, Supporting Information) and HPLC-MS (Figures S78–S80 and Tables S18–S20, Supporting Information) measurements corroborate this finding. Furthermore, HPLC-MS analysis (Figures S81–S83 and Tables S21–S23, Supporting Information) reveal the formation of a polymer $[Li_4TOBQ\text{-}Li_2S_x]_n$ ($1 < x \leq 8$, $1 \leq n$) resulting from the combination of $Li_4$TOBQ with $Li_2S_x$ (Figure S84, Supporting Information), the

decomposition product of LPSCl, similar to the reaction observed with BQ/DMBQ/TMBQ and LPSCl.

Compared with LPSCl, $Li_2S$ has a higher HOMO energy level, which is closer to the LUMO energy level of the studied quinones; therefore, it is theoretically easier to transfer the electrons from the $Li_2S$ HOMO to the LUMO of the quinone. Given that LPSCl also comprises sulfur divalent anions, based on the barrel effect, the reactivity of quinones with LPSCl may primarily hinge on their capacity to oxidize the divalent sulfur anions within LPSCl. Specifically, the ability of their LUMOs to accept electrons from the HOMO of the LPSCl. Furthermore, the reactivity of the quinones toward LPSCl significantly influences the material utilization, a pivotal factor in their suitability for application in LPSCl-based solid-state battery systems. Hence, the LUMO energy level can serve as a key descriptor for designing quinone-based molecules compatible with LPSCl-based solid-state batteries. To this end, we propose a general and straightforward principle for screening and designing quinone-based or other organic small molecules as electrode materials for LPSCl-based solid-state batteries, relying on the LUMO energy level. As illustrated in Figure 6, when the LUMO energy level of a quinone, or other organic molecule surpass the LPSCl HOMO energy level of 2.01–2.32 eV (the threshold value), their reactivity with LPSCl becomes negligible, allowing their successful application as electrode materials in LPSCl-based solid-state batteries with remarkable material utilization at room or high temperature. Notably, 2.01 and 2.32 eV represent the differences between the LUMO energy levels of TMBQ – TABQ and the HOMO energy level of LPSCl, respectively. Although the precise threshold value likely falls between, we advocate for the use of 2.32 eV as a rough estimate to ensure compatibility. Alternatively, the reactivity of a designed molecule with LPSCl can be assessed by directly comparing the LUMO energy level position with that of TABQ. The simplicity and ease of attaining the LUMO energy level make it a practical parameter to evaluate the applicability of a designed molecule to the LPSCl solid-state battery system, efficiently screening out effective molecules and avoiding material, financial, and experimental resource wastage.

## 3. Conclusion

In this work, we propose a design principle for quinone-based small molecular weight systems suitable for integration into $Li_6PS_5Cl$-based solid-state organic LMBs, and demonstrate its validity through a combination of DFT calculations and experimental analysis. The position of the LUMO energy level emerges as the key descriptor for screening and design of quinone-derivatives. For instance, when the LUMO energy level of a quinone deviates from the HOMO energy level of the argyrodite $Li_6PS_5Cl$ SSE above a certain threshold (i.e., 2.01–2.32 eV), the reactivity with $Li_6PS_5Cl$ becomes negligible. Based on this, TABQ and DABQ were successfully characterized as having good chemical stability with $Li_6PS_5Cl$ SSE and were successfully applied as active electrode materials in solid-state organic LMBs with excellent material utilization and specific energy density (at material level). We believe that the validation of key factors for designing quinone-based small molecule electrode materials will open a new avenue for the development of advanced sulfide-based solid-state organic LMBs with high efficiency and long cycle life toward practical implementation.

## 4. Experimental Section

*Chemicals and Materials*: Lithium metal chips, carbon-coated aluminum foil (Al/C) and coin cell spares (stainless steel, SS-316) were purchased from TOB new energy technology Co., Ltd. (Xiamen, China). Argyrodite $Li_6PS_5Cl$ (LPSCl) was purchased from NEI Corporation (New Jersey, USA). Carbon nanofiber (CNF) and lithium sulfide ($Li_2S$) were purchased from Merck Sigma-Aldrich. 1,4-benzoquinone (BQ), 2,5-dimethyl-1,4-benzoquinone (DMBQ), 2,3,5,6-tetramethyl-1,4-benzoquinone (TMBQ) and 2,5-dihydroxy-1,4-benzoquinone (DHBQ) were purchased from Tokyo Chemical Industry Co., Ltd. (Tokyo, Japan). 2,5-diamino-1,4-benzoquinone (DABQ) and 2,3,5,6-tetraamino-1,4-benzoquinone (TABQ) were prepared as described in a previous work.[2c,17] The composite electrodes were prepared by mixing the organic active material, LPSCl and CNF in varying weight ratios such as 15:70:15, 30:60:10, 40:55:5, and 50:47:3 for 1 h using agate mortar and pestle.

*Cell Assembly*: For the solid-state organic cell assembly, 130 mg of LPSCl SSE powder was first filled into a die with an inner diameter of 10 mm, and compressed under 1000 kg (≈128 MPa) for one min to form a pellet. Subsequently, 1.3−13.4 mg $cm^{-2}$ of the composite electrode material powder was uniformly distributed on one side of the LPSCl SSE pellet. An aluminum foil (diameter: 10 mm) was then placed over the composite electrode material powder and pressed under 4700 kg (≈600 MPa) for 5 min. The pellet was removed from the die and a lithium chip was pressed onto the opposite side of the LPSCl SSE pellet. Finally, the pellet stack consisting of composite electrode material powder, LPSCl SSE pellet and lithium chip was sealed in a CR2016 type coin cell format. All manipulations were performed inside an Ar filled glove box.

*Materials Characterization*: Powder X-ray powder diffraction (PXRD) was performed on a STOE Stadi P diffractometer in transmission geometry, equipped with a Mo anticathode (K$\alpha$ radiation, wavelength of 0.71073 Å, operating at 50 kV – 40 mA). FTIR spectroscopy was conducted using either a Bruker Alpha P or an Agilent Technologies Cary 630 spectrometer equipped with a Single reflection attenuated total reflection (ATR) module. SEM images were collected on a Zeiss Auriga cross beam workstation with Gemini SEM column. The samples for XPS analysis were prepared inside an Argon filled glove box and transferred using a controlled atmosphere vessel to the XPS instrument and directly attached to the ultra-high-vacuum system to avoid exposure to air. The XPS measurement was conducted by PHI5000 Versaprobe-II, UlVAC-PHI with an Al target working at 1486.8 kV. The peak fitting and quantitative analysis of the spectra was performed with CasaXPS software. The spectra were fitted with Doniach–Sunjic functions convoluted with a Gaussian/Lorentzian distribution and a Shirley background. High-performance liquid chromatography-mass spectrometry (HPLC-MS) measurements were performed on an ultra-high performance liquid chromatography/supercritical fluid chromatography-quadrupole time-of flight mass spectrometer (Acquity 2D-UPLC/Acquity UPC2/Xevo G2-XS QTOF, US waters) operated in both, positive and negative ion source mode. Nuclear magnetic resonance (NMR) spectroscopy measurements were conducted at room temperature on a Jeol JNM-ECZL G series spectrometer operating at a field strength of 14.1 T. Larmor frequencies: 600.09 MHz for $^1H$, and 150.91 MHz for $^{13}C$. Experiments were run under Delta 6.2 program (Jeol) using a 5 mm HFX probe equipped with a z-gradient coil.

*Electrochemical Measurements*: For the ionic conductivity measurement of the LPSCl, a 10 mm diameter Al/C disc was placed into a stainless-steel die with an inner diameter of 10 mm. Next, 130 mg of LPSCl powder was dispersed onto the Al/C foil and compressed under 1 ton (≈128 MPa) for 1 min to form a pellet. Another 10 mm diameter Al/C was then placed over the pellet and pressed under 4.7 tons (≈600 MPa) for 5 min. Finally, the pellet consisting of Al/C | LPSCl | Al/C was assembled into a Swagelok cell for electrochemical impedance spectroscopy (EIS) measurement. The related a.c. EIS was carried out by using a VMP3 electrochemical workstation (Biologic) in the frequency range from 1 MHz to 10 mHz with an

amplitude voltage of 10 mV. The ionic conductivities of solid were calculated based on the equation $\sigma = L/(R \bullet S)$, where L is the thickness of the pellet, S is the area of the surface, and R is the ionic resistance. The corresponding ionic conductivity of LPSCl is ≈3.8 mS $cm^{-1}$. The in situ EIS measurements were carried out during galvanostatic cycling at the following potentials: OCV, 2.26, 2.24, 2.15, and 1.7 V versus $Li/Li^+$ for the first discharge process, and 2.43, 2.32, 2.25, 2.15, and 1.7 V versus $Li/Li^+$ for the second and the third discharge processes; while 2.28, 2.36, 2.42, 2.53, and 2.8 V versus $Li/Li^+$ for the first charge process, and 2.27, 2.37, 2.46, 2.62, and 2.8 V versus $Li/Li^+$ for the second and the third charge processes. Each measurement was preceded by a rest period of 30 min to reach close to equilibrium conditions. An amplitude voltage of 10 mV was applied for the measurement in a frequency range from 1 MHz to 100 mHz. The galvanostatic charge–discharge tests were conducted on a Neware battery testing system (Shenzhen Neware Electron. Co. Ltd., China) at room temperature. The specific capacity and current density/rate are calculated and reported based on the mass loading of the active organic electrode materials.

*Computational Details*: The energies of the highest occupied molecular orbital (HOMO) and the lowest unoccupied molecular orbital (LUMO) were calculated by the density functional theory (DFT) implanted in Gaussian 09 software. B3LYP functional was adopted with the basis set of 6–311+G(d, p) for all the atoms.

## Supporting Information

Supporting Information is available from the Wiley Online Library or from the author.

## Acknowledgements

X.-D. L. acknowledges financial support from the Marie Skłodowska-Curie Actions (grant agreement No. 101064286) for his postdoctoral fellowship. D. R. acknowledges F.R.S.-FNRS for the Chargé de Recherché fellowship (grant agreement No. 40010410). This work was funded by INNOVIRIS 2019-RDIR-59B, F.R.S.-FNRS through grant F.4552.21-P – MIS – CSA-LION, CF-ARC grant (18/23-093) MICROBAT, European Research Council under the European Union's Horizon 2020 research and innovation program (grant agreement no.770870, MOOiRE), China Scholarship Council (H.-W. X., X.-L. G., Z.-H. C., D. T., Y. Z., Y. L., Z. L., M.-Y. D., S.-S. Y. & X.-Z. Z., PhD fellowships), the National Key Research and Development Program of China (2022YFB3803700) and the National Natural Science Foundation of China (NSFC) projects (22179112, 22072117, 22021001, 52201266) for financial support. The authors thank Dr. Chun Tang at the University of Hong Kong (Prof. J. Fraser Stoddart's group) for his instructive discussions on quinone-based molecular structure.

## Conflict of Interest

The authors declare no conflict of interest.

## Data Availability Statement

The data that support the findings of this study are available from the corresponding author upon reasonable request.

## Keywords

lithium organic batteries, organic cathodes, solid-state lithium metal batteries, sulfide electrolytes

Received: November 29, 2023
Revised: May 18, 2024
Published online:

[1] a) P. Poizot, J. Gaubicher, S. Renault, L. Dubois, Y. Liang, Y. Yao, *Chem. Rev.* **2020**, *120*, 6490; b) A. E. Lakraychi, F. Dolhem, A. Vlad, M. Becuwe, *Adv. Energy Mater.* **2021**, *11*, 2101562; c) B. Esser, F. Dolhem, M. Becuwe, P. Poizot, A. Vlad, D. Brandell, *J. Power Sources* **2021**, *482*, 228814; d) J. Wang, A. E. Lakraychi, X. Liu, L. Sieuw, C. Morari, P. Poizot, A. Vlad, *Nat. Mater.* **2021**, *20*, 665; e) J. Wang, P. Apostol, D. Rambabu, X. Guo, X. Liu, K. Robeyns, M. Du, Y. Zhang, S. Pal, R. Markowski, F. Lucaccioni, A. E. Lakraychi, C. Morari, J.-F. Gohy, D. Gupta, A. Vlad, *Sci. Adv.* *9*, eadg6079.

[2] a) Y. Wu, R. Zeng, J. Nan, D. Shu, Y. Qiu, S.-L. Chou, *Adv. Energy Mater.* **2017**, *7*, 1700278; b) X. Zhu, Y. Jing, *J. Power Sources* **2022**, *531*, 231291; c) L. Sieuw, A. Jouhara, É. Quarez, C. Auger, J.-F. Gohy, P. Poizot, A. Vlad, *Chem. Sci.* **2019**, *10*, 418.

[3] a) T. Nokami, T. Matsuo, Y. Inatomi, N. Hojo, T. Tsukagoshi, H. Yoshizawa, A. Shimizu, H. Kuramoto, K. Komae, H. Tsuyama, J.-i. Yoshida, *J. Am. Chem. Soc.* **2012**, *134*, 19694; b) Z. Song, H. Zhan, Y. Zhou, *Angew. Chem., Int. Ed.* **2010**, *49*, 8444; c) A. Vlad, K. Arnould, B. Ernould, L. Sieuw, J. Rolland, J.-F. Gohy, *J. Mater. Chem. A* **2015**, *3*, 11189; d) Z. Song, Y. Qian, X. Liu, T. Zhang, Y. Zhu, H. Yu, M. Otani, H. Zhou, *Energy Environ. Sci.* **2014**, *7*, 4077.

[4] J. Yang, P. Xiong, Y. Shi, P. Sun, Z. Wang, Z. Chen, Y. Xu, *Adv. Funct. Mater.* **2020**, *30*, 1909597.

[5] a) S. Renault, S. Gottis, A.-L. Barrès, M. Courty, O. Chauvet, F. Dolhem, P. Poizot, *Energy Environ. Sci.* **2013**, *6*, 2124; b) L. Sieuw, A. E. Lakraychi, D. Rambabu, K. Robeyns, A. Jouhara, G. Borodi, C. Morari, P. Poizot, A. Vlad, *Chem. Mater.* **2020**, *32*, 9996; c) H. Chen, M. Armand, G. Demailly, F. Dolhem, P. Poizot, J.-M. Tarascon, *ChemSusChem* **2008**, *1*, 348; d) Z. Zhu, H. Li, J. Liang, Z. Tao, J. Chen, *Chem. Commun.* **2015**, *51*, 1446; e) S. Wang, L. Wang, K. Zhang, Z. Zhu, Z. Tao, J. Chen, *Nano Lett.* **2013**, *13*, 4404; f) S. Gottis, A.-L. Barrès, F. Dolhem, P. Poizot, *ACS Appl. Mater. Interfaces* **2014**, *6*, 10870.

[6] M. Li, J. Yang, Y. Shi, Z. Chen, P. Bai, H. Su, P. Xiong, M. Cheng, J. Zhao, Y. Xu, *Adv. Mater.* **2022**, *34*, 2107226.

[7] a) A. Jaffe, A. Saldivar Valdes, H. I. Karunadasa, *Chem. Mater.* **2015**, *27*, 3568; b) B. Genorio, K. Pirnat, R. Cerc-Korosec, R. Dominko, M. Gaberscek, *Angew. Chem., Int. Ed.* **2010**, *49*, 7222.

[8] a) X. Chi, F. Hao, J. Zhang, X. Wu, Y. Zhang, S. Gheytani, Z. Wen, Y. Yao, *Nano Energy* **2019**, *62*, 718; b) F. Hao, X. Chi, Y. Liang, Y. Zhang, R. Xu, H. Guo, T. Terlier, H. Dong, K. Zhao, J. Lou, Y. Yao, *Joule* **2019**, *3*, 1349; c) L. Zhao, A. E. Lakraychi, Z. Chen, Y. Liang, Y. Yao, *ACS Energy Lett.* **2021**, *6*, 3287.

[9] a) C. Yu, S. Ganapathy, J. Hageman, L. van Eijck, E. R. H. van Eck, L. Zhang, T. Schwietert, S. Basak, E. M. Kelder, M. Wagemaker, *ACS Appl. Mater. Interfaces* **2018**, *10*, 33296; b) C. Yu, L. van Eijck, S. Ganapathy, M. Wagemaker, *Electrochim. Acta.* **2016**, *215*, 93; c) S. Wang, Y. Zhang, X. Zhang, T. Liu, Y.-H. Lin, Y. Shen, L. Li, C.-W. Nan, *ACS Appl. Mater. Interfaces* **2018**, *10*, 42279.

[10] a) F. Hao, Y. Liang, Y. Zhang, Z. Chen, J. Zhang, Q. Ai, H. Guo, Z. Fan, J. Lou, Y. Yao, *ACS Energy Lett.* **2021**, *6*, 201; b) X. Zhou, Y. Zhang, M. Shen, Z. Fang, T. Kong, W. Feng, Y. Xie, F. Wang, B. Hu, Y. Wang, *Adv. Energy Mater.* **2022**, *12*, 2103932.

[11] a) X. Gan, Z. Yang, Z. Song, *Batteries Supercaps* **2023**, *6*, 202300001; b) Z. Yang, F. Wang, Z. Hu, J. Chu, H. Zhan, X. Ai, Z. Song, *Adv. Energy Mater.* **2021**, *11*, 2102962.

[12] W. Ji, X. Zhang, L. Xin, A. Luedtke, D. Zheng, H. Huang, T. Lambert, D. Qu, *Energy Storage Mater.* **2022**, *45*, 680.

[13] a) M. Nisula, M. Karppinen, *J. Mater. Chem. A.* **2018**, *6*, 7027; b) D. H. S. Tan, E. A. Wu, H. Nguyen, Z. Chen, M. A. T. Marple, J.-M. Doux, X. Wang, H. Yang, A. Banerjee, Y. S. Meng, *ACS Energy Lett.* **2019**, *4*, 2418; c) T. K. Schwietert, V. A. Arszelewska, C. Wang, C. Yu, A. Vasileiadis, N. J. J. de Klerk, J. Hageman, T. Hupfer, I. Kerkamm, Y. Xu, E. van der Maas, E. M. Kelder, S. Ganapathy, M. Wagemaker, *Nat. Mater.* **2020**, *19*, 428; d) X. Fan, R. Yuan, J. Lei, X. Lin, P. Xu, X. Cui, L. Cao, M. Zheng, Q. Dong, *ACS Nano* **2020**, *14*, 15884.

[14] a) K. Fukui, *Science* **1982**, *218*, 747; b) L.-G. Zhuo, W. Liao, Z.-X. Yu, *Asian J. Org. Chem.* **2012**, *1*, 336; c) M. Tarumi, Y. Matsuzaki, K. Suzuki, *Chem. Eng. Sci.* **2019**, *199*, 381; d) Z. Wang, J. Liu, B. Zhang, L. Sun, L. Cong, L. Lu, A. Mauger, C. M. Julien, H. Xie, H. Sun, *Energy Storage Mater.* **2020**, *24*, 373.

[15] a) X. Guo, P. Apostol, X. Zhou, J. Wang, X. Lin, D. Rambabu, M. Du, S. Er, A. Vlad, *Energy Environ. Sci.* **2023**, *17*, 173. b) H. Kim, J. E. Kwon, B. Lee, J. Hong, M. Lee, S. Y. Park, K. Kang, *Chem. Mater.* **2015**, *27*, 7258; c) E. J. Askins, M. R. Zoric, M. Li, R. Amine, K. Amine, L. A. Curtiss, K. D. Glusac, *Nat. Chem.* **2023**, *15*, 1247.

[16] W. Zhang, T. Leichtweiß, S. P. Culver, R. Koerver, D. Das, D. A. Weber, W. G. Zeier, J. Janek, *ACS Appl. Mater. Interfaces* **2017**, *9*, 35888.

[17] D. M. Beagan, I. J. Huerfano, A. V. Polezhaev, K. G. Caulton, *Chem. Eur. J.* **2019**, *25*, 8105.